Self-induced transition between stable and thermoacoustically excited states in a gas turbine combustor

Isaac G. Boxx[1] and Klaus-Peter Geigle.[2]
German Aerospace Center, Stuttgart Germany.

Campbell D. Carter[3]
Air Force Research Laboratory, Dayton, OH

and

Jacques Lewalle[4], Ben-Akih Kumgeh[5]
Syracuse University, Syracuse NY

The goal of this study was to characterize the mechanism by which a swirl-stabilized gas turbine combustor spontaneously transitions from stable operation into a combustion mode with strong, self-excited thermoacoustic oscillation. This was accomplished by applying high-bandwidth laser- and optical imaging techniques to acquire long-duration (4s) time-series measurements of a target flame undergoing frequent, spontaneous transitions between stable und thermoacoustically excited states. The target flame was a turbulent, swirl-stabilized ethylene-air flame operated at ϕ = 0.91, and 5 bars pressure. Stereo-PIV measurements, acquired at 9.3 kHz over periods of approximately 4 seconds were used to characterize the flow-field near the exit plane of the combustor. Acoustic measurements and OH*-chemiluminescence images were acquired synchronously, with OH* images acquired at every third cycle of the PIV measurement system.

Wavelet-based analysis was employed to identify possible precursors to transition (to and from the stable state). One potential precursor was a 635 Hz oscillation that appeared $\approx$ 0.15s prior to transition. Analysis showed this oscillation to be thermoacoustic in nature and to strongly affect the outer shear layer of the flame, but the physical mechanism linking it to transition was unclear. In this study we show the physical mechanism associated with this precursor was a Helmholtz resonance that couples to the outer shear-layer of the reactant inflow, which leads to enhanced transport of hot reacting flow into the ORZ, destabilized the outer shear-layer and rendered the flame more susceptible to forcing by the (720 Hz) resonant acoustic mode of the combustor / pressure-vessel.

[1] Staff Scientist, Institute of Combustion Technology. Stuttgart, Germany. AIAA Associate Fellow.
[2] Staff Scientist, Institute of Combustion Technology. Stuttgart, Germany.
[3] Principal Aerospace Engineer, AFRL/RQHF. 1950 Fifth Street, Wright-Patterson AFB. AIAA Associate Fellow
[4] Associate Professor, Mechanical and Aerospace Engineering, 263 Link Hall, Syracuse University, Syracuse NY 13244, AIAA Member.
[5] Assistant Professor, Mechanical and Aerospace Engineering, 263 Link Hall, Syracuse University, Syracuse NY 13244, AIAA Member.

I. Introduction

To meet increasingly stringent NOx emissions regulations large-scale gas turbine power plants frequently employ swirl-stabilized, lean premixed or partially-premixed (LPP) combustors. LPP combustors achieve low NOx emissions by avoiding the high peak temperatures produced by near-stoichiometric combustion [1,2]. Unfortunately, LPP combustors are susceptible to thermoacoustic instabilities driven by the combustion process and sustained by a resonant feedback mechanism coupling pressure and heat release [1, 2, 3,4,5, 6,7, 8]. Thermoacoustic pulsation can adversely affect the performance, emissions and even structural integrity of a gas turbine power-plant.

Thermoacoustic pulsation arises out of a complex interaction between combustor and exhaust geometry, pressure, flow-field, mixing, chemical reactions, and heat-release. Despite decades of focused research on the topic, however, it remains a severe challenge to accurately predict the onset of self-excited thermoacoustic pulsation in a gas turbine combustor. While active and passive control mechanisms have been developed to reduce or eliminate thermoacoustic instabilities in various industrial burners [9, 10, 11, 12], the question of how a given swirl-stabilized flame transitions from stable operation into a state with strong, self-excited thermoacoustic pulsation remains largely unanswered. The goal of this study was to address this gap in our understanding.

In a recent study [13], we applied high-bandwidth laser-, optical and acoustic measurements to study a swirl-stabilized LPP flame in a gas turbine model combustor at engine-relevant conditions. The flame was a turbulent, swirl-stabilized ethylene-air flame operated at $\phi = 0.91$ and 5 bars pressure and thermal load of 54kW. This flame was observed to spontaneously transition between stable operation and a state with strong, self-excited thermoacoustic oscillations over periods of several seconds. These transitions were observed to occur in both directions, i.e. from stable to thermoacoustically excited and from excited to stable without a user-defined trigger or forcing. The measurements include 3-component velocity fields acquired via stereoscopic particle image velocimetry (SPIV) at 9.3 kHz over a 4 second (continuous) measurement period. OH*-chemiluminescence and OH-PLIF images were acquired synchronously at 3.1 kHz. Acoustic signals were acquired with a high-speed piezoresistive pressure transducer.

II. Apparatus

The experiment, shown schematically in Figure 1, consists of two major components; the burner, and the laser measurement system. Both of these systems have been described previously [14–17]. For the sake of completeness however, a brief description of each system is given below

Burner and Flame Condition

The burner used in this study is described in refs. [14-17]. It consists of a swirled fuel-air injector and an optically accessible combustion chamber. It is mounted in an optically accessible pressure vessel. The injector consists of two coaxial air nozzles, separated by a ring of fuel-injection channels. The inner air nozzle measures 12.3 mm in diameter. The outer (annular) air nozzle has an inner and outer diameter of 14.4 and 19.8 mm, respectively. Air for each nozzle is supplied separately, via electromechanical flow controllers (Bronkhorst). Swirl is induced in the flow through each nozzle via a set of radial swirl vanes. Gaseous fuel (C_2H_4, also set via Bronkhorst flow controllers) is injected via a ring of 60 straight channels (0.5×0.4 mm^2) located between the inner and outer nozzles. The exit planes of both the fuel and the air flows are located at the level of the combustion chamber inlet, ensuring maximal optical access to flame dynamics at the nozzle exit.

The combustion chamber measures 120 mm in height and has a square cross-section measuring 68×68 mm^2. It has four quartz windows (127 mm × 59 mm × 3 mm), yielding an optically-accessible area of 51.4 mm × 120 mm. This chamber is mounted in a water-cooled stainless steel pressure vessel with four large windows for optical access (60×120 mm^2). The chamber pressure is adjusted via a movable piston back-pressuring valve.

The burner was operated at a chamber pressure of 5 bars to produce a flame with equivalence ratio of 0.91 and thermal power of 54.2 kW. At these conditions, the combustor experiences frequent spontaneous transitions between stable- and thermoacoustically excited operational states.

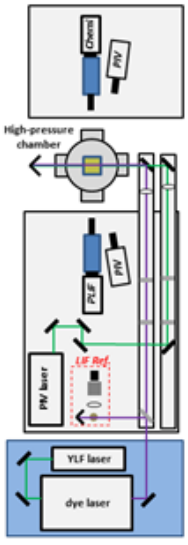

Figure 1 – Experimental Apparatus

Measurement Apparatus

The measurement apparatus used in this study consisted of a kHz acquisition-rate stereoscopic PIV system, a kHz acquisition-rate OH* chemiluminescence imaging system, a kHz acquisition-rate OH-PLIF system and a fast-response piezoresistive pressure transducer. At the time of writing, analysis of the OH-PLIF data is ongoing, and therefore these data are not included in this manuscript. These systems are described (separately) below.

Stereo-PIV System

The stereoscopic PIV system consisted of a dual-cavity, diode-pumped, solid-state Nd:YAG laser (Edgewave, IS200-2-LD) and a pair of CMOS cameras (2 × LaVision HSS8). The laser produces up to 9mJ/pulse at 532 nm at repetition rates up to 10 kHz and with pulse durations of 14 ns. The beam was formed into a laser sheet using a cylindrical telescope. Mie scattering from titanium dioxide (TiO_2) particles (nominal diameter 0.5 µm) seeded into the air flow of each nozzle was imaged using a pair of CMOS cameras. The cameras were mounted on opposite sides of the laser sheet and had sufficient on-board memory (32 GB) for up to 3.8 seconds of dual-frame PIV imaging at 9.3 kHz and 512 × 640 pixel resolution. The cameras were equipped with 100-mm focal length, f/2.8 objectives and were mounted on custom rotation fixtures and Scheimpflug adaptors. The spatial resolution of the system was 2 mm, based on the size of the PIV interrogation region (24 × 24 pixels).

OH Chemiluminescence Imaging System*

Chemiluminescence from the electronically excited OH* radical was imaged using a high-speed CMOS camera (LaVision HSS6) and external, two-stage, lens-coupled intensifier (LaVision HS-IRO) with a 45 mm focal length, f/1.8 objective (Cerco) and high-transmission, band-pass interference filter. The integration time of the intensified camera was 5 µs. The camera was operated at 512×512 pixels resolution and 3.1-kHz acquisition rate, with 8192 images (2.64 s) being acquired per imaging run.

Acoustic Measurement System

The acoustic measurement system consisted of a piezoresistive pressure transducer (Kistler 4045A20) with a natural frequency of 150 kHz and a measurement range of 0 – 20 bars, connected to a (Kistler Type 4603A) amplifier. The transducer was mounted (via a calibrated probe) to the exhaust plate of the combustion chamber. The transducer signal was read into a digital recording oscilloscope (a LeCroy HDO 6054 with 500-MHz bandwidth and 12-bit resolution ADC). The oscilloscope was used to record both the pressure transducer signal and a trigger signal from the high bandwidth imaging system. This trigger signal was used to synchronize the acoustic signal to that of the PIV, PLIF and OH* images.

III. Results

The present study focusses upon a single time-series measurement (of 4-s duration) wherein the flame was observed to transition from stable operation into a state with strong, self-excited thermoacoustic oscillation. This transition occurred at $t = 1.3$ seconds from the start of the measurement. Figure 2 (reproduced from ref. [13]) shows ensemble-averaged PIV and OH*-chemiluminescence fields for the flame in the stable (left) and excited (right) states. In the mean velocity fields, the vectors indicate direction and magnitude of the velocity. The background contour displays the magnitude of the axial component of velocity. As expected for a swirl-stabilized flame, the mean velocity fields show a conical region of high velocity reactants, an inner recirculation zone (IRZ) and an outer recirculation zone (ORZ). The IRZ results from vortex breakdown in the high-swirl reactant inflow. The ORZ results from the confinement chamber surrounding the

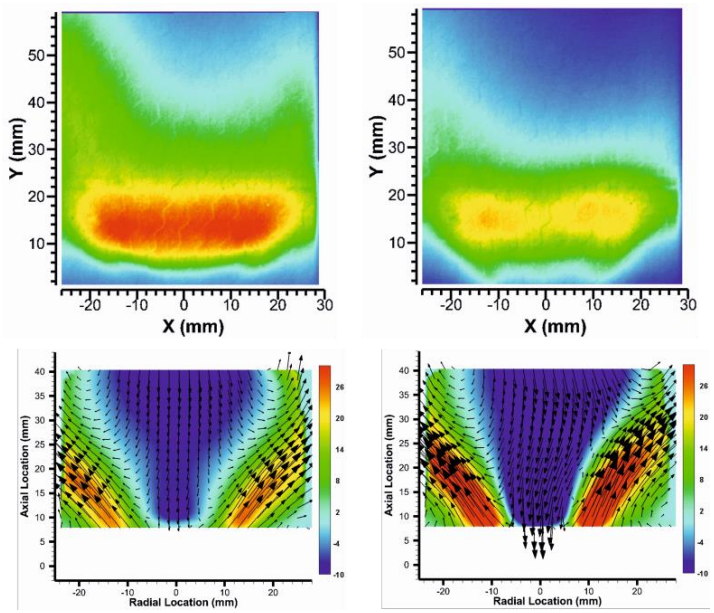

Figure 2 – Mean OH* and velocity fields of the (left) stable flame and (right) thermoacoustically excited flame. Reproduced from ref. [13]

injector. The reactants are separated from each recirculation zone by shear-layers. The mean OH* distributions indicate that in both the stable and excited states, the flame is mostly lifted from the injector nozzle. In the excited state, however, there is evidence of enhanced heat-release in the outer shear-layer. Interesting to note from these plots is how little the strong, self-excited thermoacoustic pulsations seem to affect the mean velocity and heat-release fields of the flame.

It was shown in ref. [13] that acoustic-, heat-release and velocity fields of this flame oscillated at characteristic frequencies associated with specific phenomena in the combustor. In the stable state, the dominant oscillation frequency was 472 Hz. This was observed to result from precession in the IRZ, possibly via a helical precessing vortex core (PVC). A weak (non-resonant) thermoacoustic oscillation at 610 Hz was observed to co-exist with this (primarily) fluidic oscillation. In the excited state, the dominant oscillation frequency was observed to be a strong, self-excited thermoacoustic pulsation at 720 Hz. When this pulsation appeared at approximately $t = 1.3\ s$, it immediately became the dominant feature in the acoustic-, heat-release and velocity-field measurements.

These frequencies are identifiable in power spectra of the stationary states, which eliminate temporal resolution and assume infinite harmonic oscillation. A useful tool for identifying transient phenomena associated with unpredictable events like stable-to-excited transitions in a swirl flame is the wavelet transform. In this study, we apply the continuous wavelet transform to "zoom in" on frequency content of the signal around the time of the stable-to-excited transition. Thorough presentations on continuous wavelets can be found in refs. [18, 19]. The wavelet transform is the convolution of the wavelet with the signal $u(t)$:

$$\tilde{u}(f,t) = \int_{-\infty}^{\infty} u(t')\psi^*(f, t-t')dt'$$

The plot of this function's contour lines in a time-frequency domain is called a scalogram; its value at a particular time and frequency is a wavelet coefficient. Denoting the Fourier transform by

$$\hat{u}(f) = \int u(t)\exp(-2i\pi ft)dt\ ;$$

the wavelet transform can also be expressed as a band-pass filtered signal, with the wavelet determining the shape of the frequency band, since

$$\tilde{u}(f,t) = \int \hat{u}(\omega)\hat{\psi}^*(\frac{\omega}{f})\exp(2i\pi\omega t)\,\mathrm{d}\,\omega\ .$$

The *norm* of the Morlet coefficients can be interpreted as the envelope of the fluctuations at a given frequency, and the real part is a representation of the fluctuations inside the envelope.

Figure 3 (reproduced from ref. [13]) shows the envelope scalogram of the axial velocity field measured during a 0.4 s period straddling the transition from the stable to the excited state. The horizontal and vertical axes represent time and frequency, respectively. Darker shades correspond to more energetic fluctuations. The dominant oscillation frequencies described above are highlighted on this plot via colored lines. Scalograms were also computed for the acoustic- and OH*-chemiluminescence data and showed consistent activity within each frequency range. Of particular interest in Figure 3 is the presence of a short-lived, 635 Hz oscillation in the signal that appears at $t \approx 1.15\ s$ and persists until $t \approx 1.3\ s$, when the 720 Hz thermoacoustic oscillation appears and becomes the dominant oscillation mode. This oscillation was identified in ref. [13], but the mechanism responsible for it was unclear.

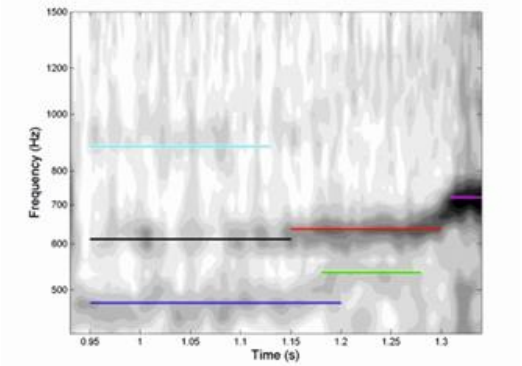

Figure 3. Morlet-amplitude (envelope) scalogram for axial velocity in the flame region.

Definition of Phase from Complex Wavelet Coefficients.

In addition to the standard wavelet-based tools such as scalograms, spectra and frequency-resolved correlations, the Syracuse group has recently made use of pattern recognition and the definition of phase in broadband signals [20-22]. Phase is uniquely adapted to the current data, because of the local periodicity of the various modes.

At any frequency, the phase angle between the imaginary and real parts of the Morlet wavelet coefficients gives a value that coincides with the phase of a Fourier wave in the limit of periodic signals. We adopt it as our definition of phase for broadband signals as well. In the time-frequency domain, there will be few cycles at low frequencies and more cycles at higher frequencies, and the scalogram of phase will necessarily branch out, as seen in Figure 4 (which is shown as a good example but is unrelated to this study).

Therefore, we can assign a phase value in the time-frequency domain, without the need for an external reference or for perfect sinusoidal oscillations. We will focus on the frequencies of the oscillatory modes involved in the transition process (475, 635 and 720 Hz), during the relevant time brackets. Phase depends on frequency, time and spatial location, and therefore we need to perform sections and projections (statistics) through this space in order to expose useful information.

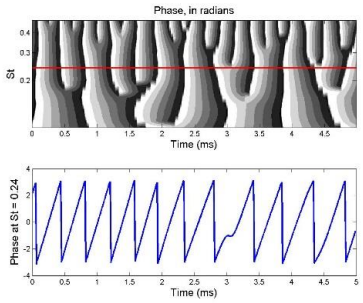

Figure 4. Time-frequency phase of a broadband signal [20], phase at one frequency.

Phase Distribution at 720Hz

Starting with the dominant excited mode, which is very active in the upper half of the measurement region, we took the phase of the axial velocity component at the exhaust centerline as reference, and we subtracted it from the phase at all points in the field. Because the color scale shows an abrupt change from red to blue as the phase crosses 2π, we shifted all phases by π to de-emphasize small phase changes around 0. At various x-locations in the burner, the phase distribution is as shown in Figure 5.

First, looking at the post-flame region ($x > \approx 20$ mm) we note that for $t < 1.3$ *s*, the 720-Hz reference is physically irrelevant, and not better than random: this is reflected in the variegated colors for the stable state with this reference. After transition to the excited state, however, we see that the entire field for $x > 26$mm is in phase with the reference, as expressed by the yellow-green contour lines. Thus we can conclude that the thermoacoustic fluctuations in the upper half of the burner are stationary waves, as would be expected in relation to a Helmholtz resonator (between the combustor and plenum**)** [23]**.** At lower positions in the burner, consistent bands appear in the y direction. These bands change color as the x location varies, indicating propagating waves; however, the location of the bands does not change in the region $10.9 < x < 19$ mm. The blue contours along the centerline ($|y| < 5$ mm) at the location shown denote phase opposition relative to the exhaust; then regions about 10 mm on either side are populated by yellow and green contours, almost consistent with the reference phase; and for $|y| > 17$ mm, yellow contours return, but after covering the entire phase scale (yellow-blue-red-yellow). At yet lower sections (e.g., $x =$ 7.9 mm) the band closest to the centerline disappears, leaving an inner region (presumably the jet) with yellow-red-coded phases, and outer regions with blue-green dominance.

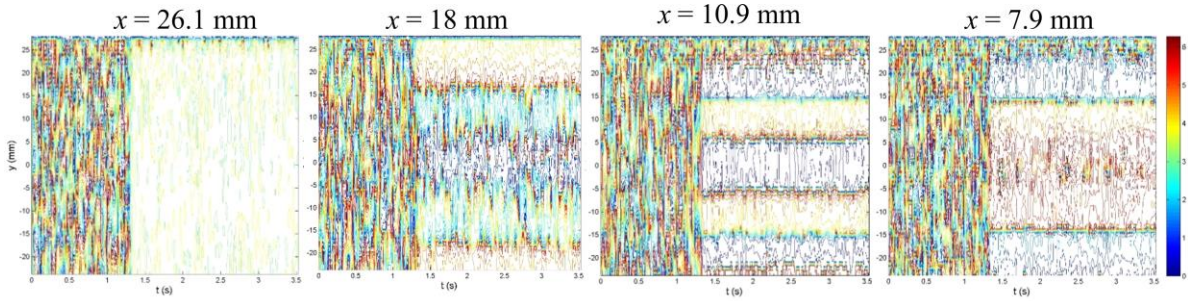

Figure 5 Successive axial sections (x location as labelled) of the phase (relative to centerline exhaust phase) as functions of time and spanwise location. The phase is shifted by π to enhance the continuity of phases values in the green-yellow part of the color bar.

Phase Distribution at 635 Hz

Figure 6 shows the distribution of phase in the data relative to the 635-Hz oscillation. This plot shows the 635-Hz mode affects the flow in much the same way as the 720-Hz mode. In the period from $t = 1.15$ *s* to $t = 1.3$ *s*, one sees similar uniformity of phase in the axial velocity in the post-flame regions ($x > 23$mm). Consistent also with

behavior of the 720-Hz mode, consistent bands appear in the y direction closer to the burner face. The location of the bands does not change in the region $10.9 < x < 19$ mm. This illustrates that during the period $t = 1.15 - 1.3$ *s*, the 635-Hz mode affects the flow in a manner similar to that of the subsequent 720-Hz (thermoacoustic) mode. The similarity in phase distribution across the combustor suggests a similar origin for the two modes, i.e. a Helmholtz resonance.

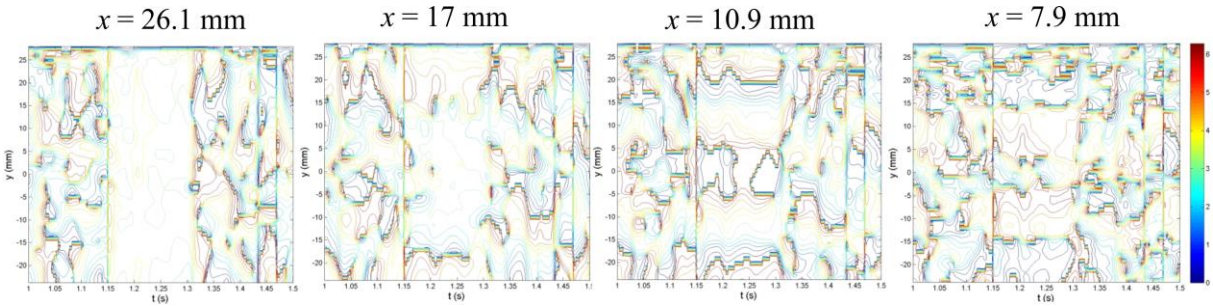

Figure 6 – Successive axial sections of the phase (relative to 635-Hz oscillation) as functions of time and spanwise location. Phase is shifted by π to enhance the continuity of phases values in the green-yellow part of the color bar.

As a result, phase emerges as a dependable statistic in our analysis; in this data, it will be a function of time (including conditional on stable, transition or excited state), frequency and spatial location. We will now do sections and statistical projections of this 4-D space to expose some of the physics of the oscillatory modes. First, we perform time averages of the phase; then we turn to phase-averaged velocity, much smoother than the frequency-filtered instantaneous oscillations. This reveals a pattern in the shear-layer oscillations consistent with the OH* chemiluminescence data in the ORZ.

Mean Phase Distribution

Figure 7a shows the time-average of phase at 720 Hz, across the entire velocity field. Again, zero phase relative to the exhaust is shifted by π, so the regions in phase with the reference point will remain at the center of the scale (white contours). The time average is calculated only over the excited state, i.e. for $t > 1.3$ *s*. The results in this figure are consistent with the time-series of the relative phase presented in Figure 6. We see that the upper half of the field ($x > 20$ mm) is in phase with the reference point, indicating the stationary wave associated with the Helmholtz resonator. Closer to the burner face, one sees the phase gradually increase, both along the axial centerline of the burner and towards the walls. This axially symmetric distribution of phase is consistent with the bands seen at the same height above the burner in Figure 6. Increasing relative phase in this figure is indicative of wave propagation, with the phase velocity as the gradient of the phase. Comparing this figure with the mean velocity field shown in Figure 3, this wave propagation is clearly indicative of the thermoacoustic pulsation coupling with the reactant inflow.

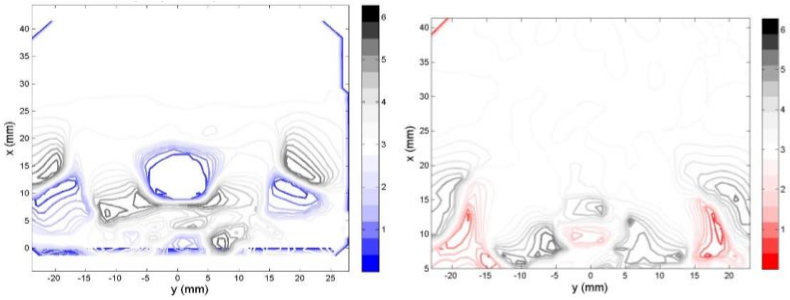

Figure 7. Relative Phase of Mean Axial velocity field. A) 720 Hz, b) 635 Hz

Figure 7b shows the time average of phase at 635 Hz, calculated over the interval $t = 1.15$ - 1.3 *s*. immediately obvious is the similarity between the relative phase distributions for the 635- and 720-Hz modes. This reinforces the conclusion that the 635-Hz mode results from the same mechanism as the 720-Hz mode. In contrast with Figure 7a however, one sees greater phase variation in outer shear- layer and near the combustion chamber windows in the 635-Hz mode than in the 720-Hz mode. This suggests that, whereas the 720-Hz mode strongly affects flow throughout the combustion chamber, the effect of the 635-Hz oscillation is primarily felt in the outer shear layer and where the flame impinges on the combustor wall. The difference in phase-distribution between these two thermoacoustic oscillations is not unexpected given that one acts upon a stable flame, which has very different damping characteristics than the excited flame.

Phase-Averaged Velocity Fields

Figure 8 shows plots of axial velocity fluctuations measured in the burner, phase-averaged with respect to the 635- and 720-Hz thermoacoustic oscillations. The reference signal was the exhaust pressure. The band-pass filtered velocity data were phase-averaged with respect to the 635-Hz oscillation over the interval *t=1.15 – 1.3 s* (immediately prior to transition), and the 720-Hz oscillation over the interval *t=1.3 – 1.45 s* (immediately after the flame transitions to the excited state). The plots are somewhat noisy due to the fact that the velocity fields were sorted into 12 phase bins, and 0.15 s corresponds to approximately 1400 measurements acquired over 95 or 108 cycles of the 635- and 720-Hz oscillations, respectively. Therefore, each phase-averaged image represents approximately 115 measurements. Nonetheless, these averages reveal clear similarities and differences in the effect of these two modes on the flow field.

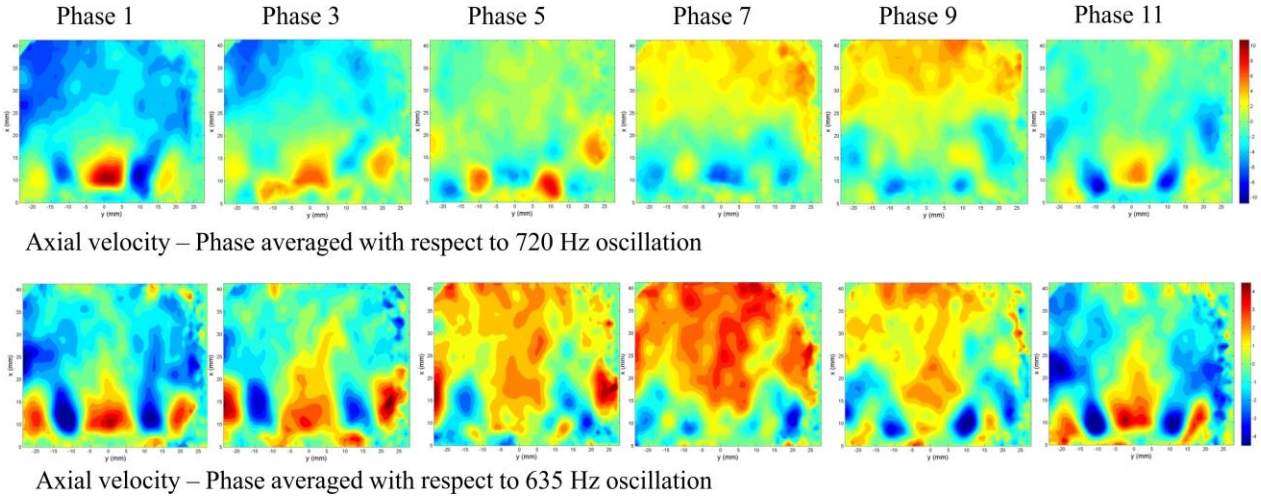

Figure 8. Phase averaged axial velocity

Beginning with the 720-Hz oscillation, one sees the axial velocity fluctuations in the post-flame region (x > 20 mm) remain fairly uniform across the width of the combustor and vary from strongly negative at Phase 1, to neutral at Phase 5, positive at Phase 9 and back neutral at Phase 11. A similar oscillation is observed in the IRZ, albeit with the sign of the fluctuation reversed. This is consistent with a Helmholtz resonance mode. The periodic fluctuations observed in the shear-layer between the reactant inflow and the IRZ are consistent with the phase distributions presented in Figure 6, inasmuch as one sees virtually no variation in phase across the width of the burner at heights above x = 20 mm, but axially-symmetric variation in phase below that height.

The phase-averaged data in Figure 8 indicates the effect of the 635-Hz oscillation is weaker and more spatially localized than that of the 720-Hz mode. Whereas the 720-Hz mode affects the flow relatively uniformly across the width of the combustor in the post-flame fluid (x > 20mm), the 635-Hz oscillation appears to act more strongly along the burner centerline than at the burner walls. This is consistent with the mean relative phase data plotted in Figure 7, which shows relatively little phase variation along the burner centerline and much stronger variation near the combustor wall. The 635-Hz oscillation also has a much weaker influence on the high momentum reactant inflow near the nozzle than does the 720-Hz mode.

Figure 9 shows plots of radial velocity fluctuations phase-averaged with respect to the 635- and 720-Hz thermoacoustic oscillations. As with the axial velocity fluctuations plotted in Figure 8, the 635 -Hz and 720-Hz phase-averages were computed for the periods *t=1.15 – 1.3 s* and *t=1.3 – 1.45 s*, respectively. Figure 9 illustrates clear similarities and important differences in how each oscillation affects the flow. In the case of the 720-Hz oscillation, the radial velocity fluctuations overlap well with the reactant inflow. This is consistent with previous studies [17], which indicate that in the excited state, the thermoacoustic pulsation couples with the shear-layer and induces periodic shedding of ring vortices in the shear-layer at the thermoacoustic oscillation frequency. In contrast, the radial velocity fluctuations associated with the 635-Hz oscillation overlap primarily with the outer shear-layer of the reactant inflow. Indeed, the strongest radial velocity fluctuations associated with this mode lie directly in the ORZ.

The phase-averaged velocity fluctuations indicate that although the 635- and 720-Hz oscillations are both thermoacoustic in nature, they affect the flow in considerably different ways. The 720Hz oscillation is associated with strong axial pulsation and the shedding of axially-symmetric ring vortices at the injector exit. The 635-Hz

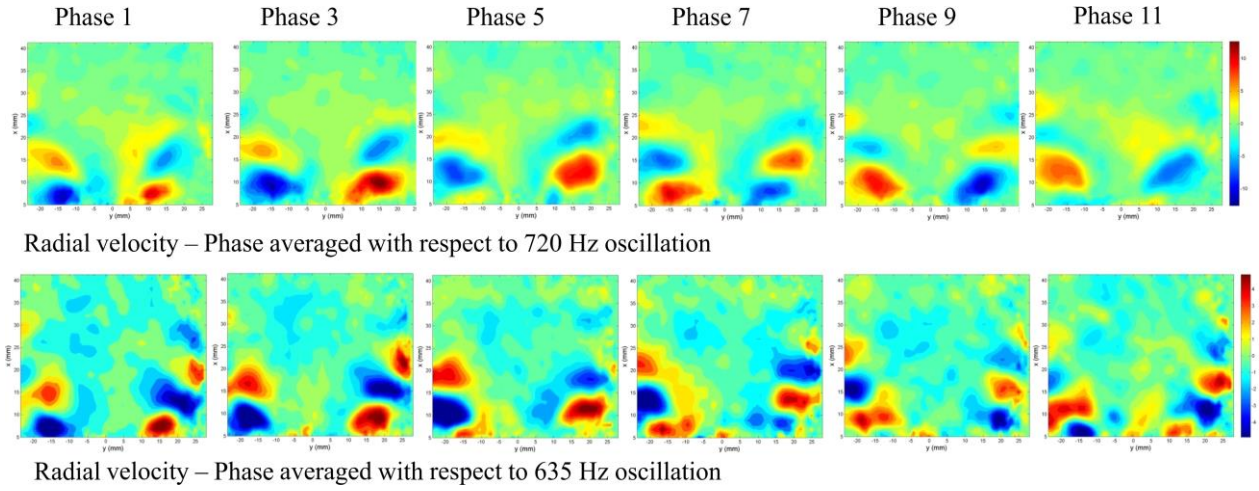

Figure 9. Phase averaged radial velocity

mode, on the other hand, is associated with relatively weak axial pulsation along the burner centerline and strong radial pulsation in the ORZ. This pulsation extends to the impingement point of the flame with the combustor wall and may reasonably be expected to lead to enhanced transport of hot, combusting material into the ORZ.

OH Chemiluminescence in the ORZ Prior to Transition*

Figure 10 presents OH* chemiluminescence measurements, ensemble-averaged over 0.15s prior to, during and after the flame transition. Although computed over a shorter period, the averages corresponding to the stable and the excited flame are consistent with those in Figure 2. In both the stable and the excited state, there is minimal OH* in the ORZ. During the 0.15s leading up to the transition, however, one sees a significant concentration of OH* in the ORZ. This suggests the presence of hot, reacting fluid in the ORZ is a contributing factor in the transition from the stable to the excited state. To more fully understand the role of this hot gas in affecting flame transition, it is important to know how the fluid arrives there. That is, whether it results from a gradual build-up over a prolonged period or if it is transported there in a single, strong influx.

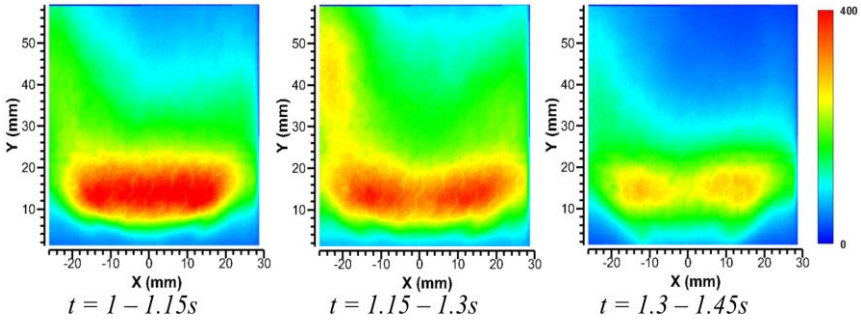

Figure 10. Ensemble averaged OH chemiluminescence measurements*

The time-series of mean OH* chemiluminescence measured in the ORZ on one side of the measurement frame is presented in Figure 11. In this figure, the instantaneous value is plotted in blue and a 50-point (0.02s) running average is overlaid in red. In this figure, we see the mean OH* signal in the ORZ is approximately 80 counts during the period of stable operation and 60 counts in the excited state. In the stable flame ($t < 1.15$ *s*) one observes regular bursts of OH* chemiluminescence in the ORZ. Although large in magnitude, these bursts tend to be of short duration. In the excited flame, one observes only small-magnitude fluctuations of OH* in the ORZ. During the 0.15 s

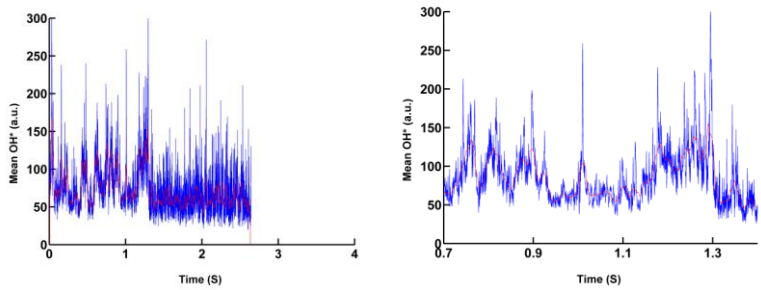

Figure 11. Mean OH Chemiluminescence measured in the left ORZ*

immediately prior to transition, however, one observes a fairly consistent growth in ORZ OH*. The peak OH* signals during this period are not significantly higher than those seen during earlier in the time series. What distinguishes this period is the persistence of the increased OH* signal, which suggests a gradual accumulation of hot, reacting gas in the ORZ rather than a single, sudden influx.

To better understand the correlation between the gradual increase of OH* chemiluminescence and oscillation in the ORZ, we computed a spatial average of the Morlet coefficients over a 7 × 7 point region in the ORZ for each point in time. Averaging the Morlet coefficients has the effect of highlighting local (spatial) phase coherence, while retaining temporal resolution. The resulting scalogram is presented in Figure 12, together with corresponding OH* signal measured in the ORZ. It is clear from this figure that the appearance of the 635-Hz oscillation corresponds temporally with the increase in OH* that eventually leads to flame transition. It also overlaps with the final disappearance of the 472-Hz oscillation known to be associated with precession of the IRZ. This rules out the possibility that the increase in OH* in the ORZ prior to transition is results from the precessing structure in the IRZ.

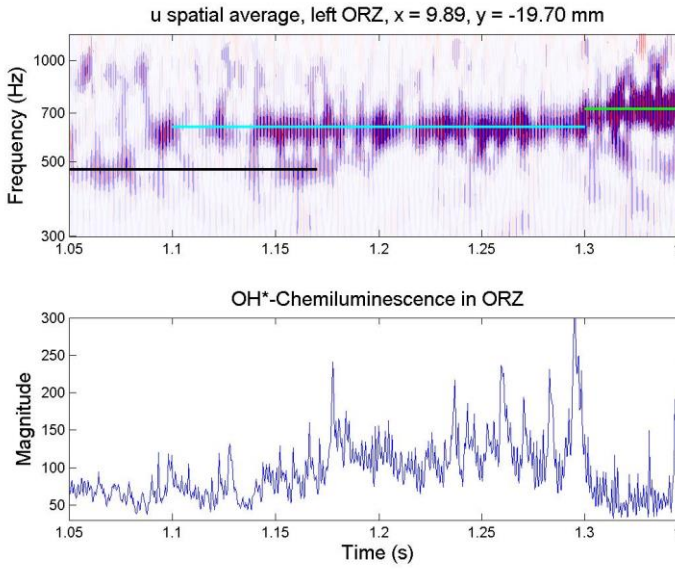

Figure 12. Local signal coherence vs. OH in the left ORZ prior to transition*

IV. Discussion

The time-frequency analysis presented above indicates the stable-to-excited state transition in this combustor is preceded by a 635-Hz oscillation that persists for approximately 0.15s. This oscillation is thermoacoustic in nature but relatively weak compared to that of the 720-Hz oscillation present in the excited state. The 635-Hz oscillation primarily affects flow along the burner centerline, the outer shear-layer and the ORZ. It appears to have a more limited impact on the inner shear-layer or high-velocity reactant inflow. Concomitant with the appearance of the 635-Hz oscillation, there is a gradual but persistent increase in hot, reacting fluid in the ORZ.

Taken together, this indicates the stable-to-excited state transition observed in this study was the result of a weak thermoacoustic oscillation (635 Hz) coupling with the reactant inflow to induce strong, coherent velocity fluctuations in the ORZ. This led to enhanced transport of hot, reacting gas into the ORZ, which destabilizes the outer shear-layer. Without the stabilizing influence of the outer shear-layer, the flame is more susceptible to forcing from resonant acoustic modes in the combustor and almost immediately transitions to the excited state.

V. Conclusion

In this study, high-bandwidth, laser- and optical imaging and acoustic measurements were used to identify and characterize the thermal-/physical mechanism by which a swirl-stabilized gas turbine combustor spontaneously transitions from a stable operating condition to one with strong, self-excited thermoacoustic oscillation. A wavelet-based analysis of the time-series data acquired in this study revealed the onset of a coherent, 635-Hz oscillation in the combustor approximately 0.15 seconds prior to the combustor transitioning into the thermoacoustically excited state. Analysis shows this oscillation is thermoacoustic in nature and originates in the exhaust section of the combustor. Phase-averaging the data shows that this oscillation induces strong radial fluctuations near the combustor walls that are accompanied by a gradual increase in OH* chemiluminescence in the ORZ.

Taken together, our analysis indicates that the stable-to-excited state transition observed in this study results from the coupling of a 635-Hz resonance in the exhaust of the combustor and the outer shear-layer of the reactant inflow. That leads to the transport of hot reacting flow into the ORZ, which appears to destabilizes the outer shear-layer. Absent the stabilizing effect of the outer shear-layer, the flame becomes more susceptible to forcing by the

(720-Hz) resonant acoustic mode of the combustor / pressure-vessel and immediately transitions into the excited state.

Although the analysis presented in this paper is limited to a single transition event, this mechanism for stable-to-excited state transition has not been previously observed in this well-characterized combustor. This is indicative of the potential of combining high-bandwidth laser and optical imaging techniques with time-frequency analysis to study unpredictable "outlier" events in turbulent flames. A fuller statistical analysis of the many, long-duration time-series measurements acquired in this study is currently in progress.

Acknowledgments

This material is based upon work supported by the Air Force Office of Scientific Research, Air Force Material Command, USAF under Award No. FA9550-16-1-0044.

C. Carter was supported under the Air Force Windows on the World program.

References

1. S. Correa. Proc. Comb. Inst. (1998) 1793-1807.
2. A.H. Lefebvre, Gas Turbine Combustion, Taylor & Francis, Philadelphia, 1999
3. J.J. Keller, AIAA J. 33 (1995) 2280-2287.
4. E.C. Fernandes, M.V. Heitor, in F. Culick, M.V. Heitor, J.H. Whitelaw (Eds.), Unsteady Combustion, Kluwer Academic press, Dordrecht, 1996.
5. C.O. Paschereit, E. Gutmark, W. Weisenstein, Combust. Sci. Technol. 138 (1998) 213-232.
6. S. Candel. Proc. Comb. Inst. 29 (2002) 1-28.
7. J.G. Lee, D.A. Santavicca, J. Propulsion and Power 19 (2003) 735-750.
8. T. Lieuwen, V. Yang. Combustion Instabilities in Gas Turbine Engines: Operational Experience, Fundamental Mechanisms, And Modeling, AIAA (2005).
9. N. Docquier, S. Candel, Prog. Energy Combust. Sci. 28 (2002) 107-150.
10. I. Emiris, J.H. Whitelaw, Combust. Sci. Technol. 175 (2003) 157-184.
11. G.A. Richards, D.L. Straub, E.H. Robey, J. Propulsion Power 19 (2003) 795-810.
12. H.C. Mongia, T.J. Held, G.C. Hsiao, R.P. Pandalai, J. Propulsion and Power 19 (2003) 822-829.
13. I.G. Boxx, K.-P. Geigle, C.D. Carter, J. Lewalle, B. Kumgeh. GT2017-64438. Proceeding of ASME 2017. Turbo Expo IGTI 17. June 26-30, 2017, Charlotte, North Carolina, USA (Under Review)
14. K.P. Geigle, R. Hadef, W. Meier. J. Eng. Gas Turbines Power 136 (2014) 021505.
15. K.P. Geigle, M. Köhler, W. O'Loughlin, W. Meier. Proc. Comb. Inst. 35 (2015) 3373.
16. I.G. Boxx, C.D. Carter, K.-P.Geigle, W. Meier., 54th AIAA Aerospace Sciences Meeting, AIAA SciTech Forum, AIAA 2016-0435.
17. I.G. Boxx, C.D. Carter, K.-P. Geigle, W.Meier. 18th International Symposium on the Application of Laser and Imaging Techniques to Fluid Mechanics. Lisbon, Portugal. July 4 – 7, 2016.
18. S. Mallat, A Wavelet Tour of Signal Processing, Academic Press 1998
19. J. Lewalle, M. Farge and K. Schneider, Wavelets, in *Springer Handbook of Experimental Fluid Mechanics*, Springer Verlag, 2007.
20. Kan, P., Ruscher, C.J, Lewalle, J., Gogineni, S. and Kiel, B.V., The Pressure Field in a Supersonic 3-Stream Jet Flow, Part II, the Near Field, (*under review*) AIAA Journal, 2016;
21. Kan, P., Ruscher, C. J., Lewalle, J., Glauser, M. N., Gogineni, S. & Kiel, B. V., 'Extracting Near-Field Structures Related to Noise Production of High Speed Jets', 54th Aerospace Sciences Meeting, AIAA SciTech, San Diego, CA, USA, 2016;
22. Lewalle,J., Kan, P., Ruscher, C.J., Glauser, M.N., Gogineni, S. and Kiel, B.V., Correlation of events between near- and far-field of a 3-stream supersonic nozzle, paper 2321277 SciTech, January 5, 2016.
23. A.D. Pierce, Acoustics, Acoustical Society of America, 1994;